

# 1 Evolution of Structural Order and Magnetic Anisotropy in 2 $\text{Yb}_{0.5}(\text{Co}_{1-x}\text{Fe}_x)_3\text{Ge}_3$ through Doping of a Kagome Lattice

3 Rahul Meduri, Mario A. Plata, Gregory T. McCandless, Benny C. Schundelmier, Mehak Ghafoor,  
4 Kaya Wei, and Julia Y. Chan\*



Cite This: <https://doi.org/10.1021/acs.chemmater.5c00119>



Read Online

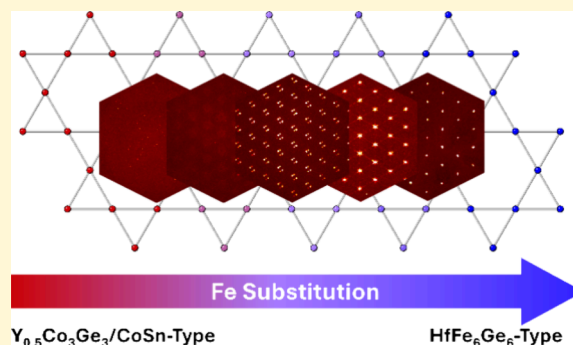
ACCESS |

 Metrics & More

 Article Recommendations

 Supporting Information

5 **ABSTRACT:** Kagome materials provide fruitful grounds for exploring  
6 the intersection of topology and magnetism. In this article, the single  
7 crystal growth of  $\text{Yb}_{0.5}(\text{Co}_{1-x}\text{Fe}_x)_3\text{Ge}_3$  ( $x = 0.00, 0.25, 0.50, 0.75,$  and  
8  $1.00$ ) is reported. As Fe is substituted into the Co-containing kagome net,  
9 the structure transforms from the disordered  $\text{Y}_{0.5}\text{Co}_3\text{Ge}_3/\text{CoSn}$ -type  
10 hybrid structure to the ordered  $\text{HfFe}_6\text{Ge}_6$ -type structure. Diffusive  
11 scattering is observed in all doped concentrations that eventually  
12 converge to a single reflection in the Fe end member, ultimately  
13 doubling the unit cell along the  $c$ -axis. Anisotropic magnetic measure-  
14 ments were performed to evaluate how the magnetism of the kagome  
15 lattice is influenced by Fe substitution. Magnetic interactions are  
16 primarily observed along the  $c$ -axis. Additionally, a reorientation of the  
17 magnetic easy axis is observed with increasing Fe incorporation,  
18 highlighting how the magnetism of this material can be chemically tuned. Resistivity with unusual behavior observed in the  
19 doped compositions is also reported. The rationale behind the structural evolution from disordered to ordered is discussed.



## 20 ■ INTRODUCTION

21 Materials with a kagome sublattice consisting of a transition  
22 metal have sparked much interest in the condensed matter  
23 community due to the exotic quantum states and various  
24 topological band features present.<sup>1,2</sup> The  $\text{AV}_3\text{Sb}_5$  ( $A = \text{K}, \text{Rb},$   
25 and  $\text{Cs}$ ) family of compounds<sup>3</sup> has displayed charge density  
26 waves (CDWs),<sup>4</sup> superconductivity,<sup>5</sup> and an anomalous Hall  
27 effect.<sup>6,7</sup> The CDWs in  $\text{CsV}_3\text{Sb}_5$  have been associated with an  
28 orthorhombic distortion of the kagome lattice, resulting in the  
29 doubling of the unit cell.<sup>8,9</sup> Alternatively, the mechanisms for  
30 CDWs observed in  $\text{FeGe}$  have shown to be primarily separate  
31 from the kagome net.<sup>10,11</sup> Annealing studies of  $\text{FeGe}$  show that  
32 the decrease in disordered structural features promotes CDW  
33 formation.<sup>12</sup>  $\text{Fe}_3\text{Sn}_2$  has displayed room temperature sky-  
34 rmions and an anomalous Hall effect.<sup>13,14</sup>  $\text{Co}_3\text{Sn}_2\text{S}_2$  is a  
35 ferromagnet (Curie temperature = 180 K) that has also  
36 displayed a large anomalous Hall effect caused by magnetic  
37 Weyl Fermions positioned near the Fermi level.<sup>15–17</sup>  
38 Members of the intermetallic  $\text{AM}_6\text{X}_6$  ( $A =$  electropositive  
39 element,  $M =$  transition metal,  $X =$  main group element) family  
40 are another group of kagome materials that host a diverse array  
41 of electronic interactions that are fruitful in realizing new  
42 technologies, often owing to the strong exchange interaction of  
43 the rare-earth element and the transition metal.<sup>18</sup>  $\text{ScV}_6\text{Sn}_6$  and  
44  $\text{LuNb}_6\text{Sn}_6$  have both shown density wave ordering.<sup>19,20</sup> A  
45 rattling mode of elements occupying the  $c$ -axis was proposed to  
46 be the mechanism behind charge ordering. A study that doped

Sc with the larger Y and Lu shows that with increasing 47  
chemical pressure along the  $c$ -axis, the CDW transition is 48  
suppressed.<sup>21</sup>  $\text{AM}_6\text{X}_6$  compounds where  $M = \text{Mn}, \text{Fe}$  are the 49  
only analogs to have been reported to possess high- 50  
temperature magnetic ordering in the kagome lattice<sup>22</sup> and 51  
give way to complex long-range magnetic structures, namely, 52  
with  $M = \text{Mn}$ .<sup>23–26</sup> Figure 1 shows the structure of 53  
 $\text{Yb}_{0.5}\text{Co}_3\text{Ge}_3$ , a disordered variant of compounds in the 54  
 $\text{AM}_6\text{X}_6$  family that adopts a hybrid of the two structure 55  
types,  $\text{Y}_{0.5}\text{Co}_3\text{Ge}_3$  and  $\text{CoSn}$ , that our group previously 56  
reported.<sup>27</sup> A Curie–Weiss fit to the magnetic susceptibility 57  
yielded an effective moment ( $\mu_{\text{eff}}$ ) of  $4.23 \mu_B$  with negative 58  
Weiss constants and no long-range magnetic ordering above 2 59  
K, suggesting magnetic frustration. A higher magnetization was 60  
observed for  $H/c$ , giving rise to anisotropic magnetism within 61  
this compound. A feature around 25 K was also observed in 62  
the  $H // a$  data reminiscent of spin-canting or that a spin 63  
reorientation has occurred.<sup>27</sup> Data collection at 50 K revealed 64  
superlattice reflections warranting a doubling of the  $c$ -axis and 65  
a change in space group from  $P6/mmm$  to  $P6_3/m$ .<sup>28</sup> Unlike the 66

Received: January 15, 2025

Revised: February 27, 2025

Accepted: February 28, 2025

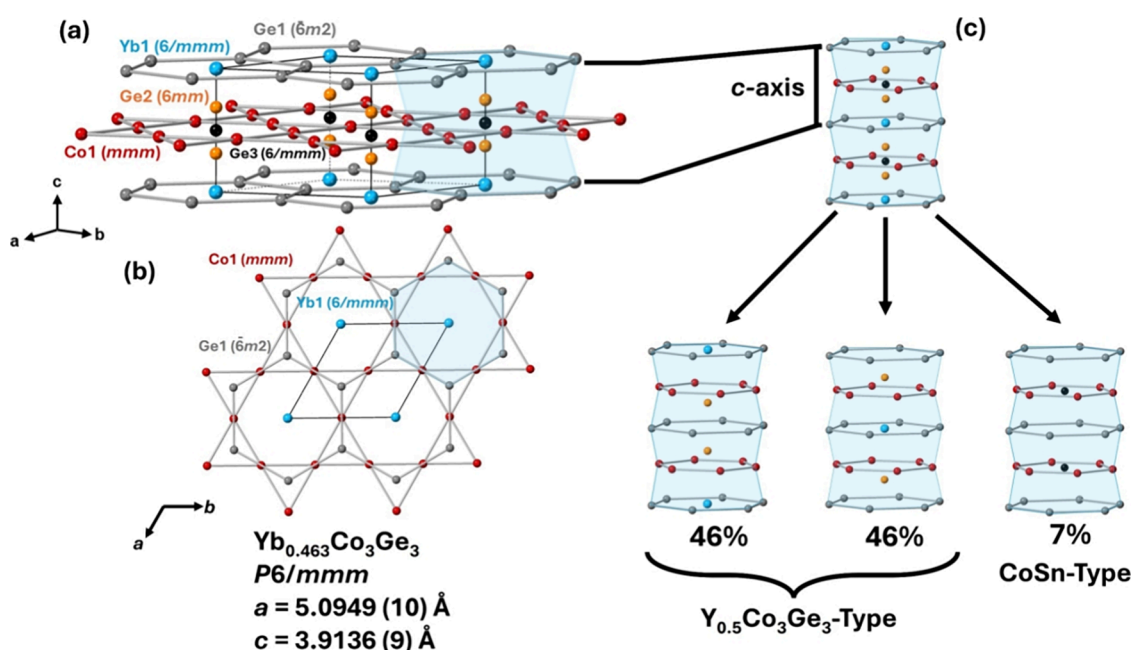


**Figure 1.** Previously reported structure of Yb<sub>0.5</sub>Co<sub>3</sub>Ge<sub>3</sub> with selected bonds omitted to emphasize the alternating stack of honeycomb nets and kagome nets along the *c*-axis.<sup>18</sup> (a) Full unit cell view. (b) View along the *c*-axis. (c) Structural motifs deconstructed with respective occupancies.

67 structural phase transitions seen in other kagome metals, with  
 68 buckling of nets at low temperatures,<sup>29</sup> an in-plane twisting of  
 69 the kagome lattice was discovered similar to what was reported  
 70 with MgCo<sub>6</sub>Ge<sub>6</sub>.<sup>30</sup> The kagome distortion coincides with a  
 71 kink in the resistivity observed around 95 K.<sup>28</sup> Additionally,  
 72 anisotropic negative magnetoresistance was observed, further  
 73 highlighting the anisotropy of this material. A related analog  
 74 adopting the HfFe<sub>6</sub>Ge<sub>6</sub> structure type, YbFe<sub>6</sub>Ge<sub>6</sub> exhibits a  
 75 magnetic spin reorientation at around 63 K, shifting the easy  
 76 axis from *a* to *c*.<sup>31</sup> The Y<sub>0.5</sub>Co<sub>3</sub>Ge<sub>3</sub>-type polymorph of  
 77 YbFe<sub>6</sub>Ge<sub>6</sub> does not display this reorientation and it is still  
 78 unknown why this occurs.<sup>32</sup>

79 Herein, we report the single crystal growth and character-  
 80 ization of Fe-doped Yb<sub>0.5</sub>Co<sub>3</sub>Ge<sub>3</sub>, as well as the change in  
 81 magnetic and electrical properties with Fe substitution. In  
 82 addition, the end members (*x* = 0.00 and 1.00) were also  
 83 grown to compare the structural and physical property  
 84 differences. The compounds were grown out of Sn flux and  
 85 the structure and elemental compositions were determined  
 86 using single crystal X-ray diffraction (SCXRD) and energy-  
 87 dispersive (X-ray) spectroscopy (EDS). Increasing Fe sub-  
 88 stitution (*x* ≥ 0.50) into the kagome sublattice results in  
 89 structural order in the form similar to the HfFe<sub>6</sub>Ge<sub>6</sub>.  
 90 Additionally, small amounts of Sn incorporation were detected  
 91 from EDS. However, for simplicity, the nominal composition  
 92 for all compounds will be referred to as Yb<sub>0.5</sub>(Co<sub>1-x</sub>Fe<sub>x</sub>)<sub>3</sub>Ge<sub>3</sub> (*x*  
 93 = 0.00, 0.25, 0.50, 0.75, 1.00). Magnetic behavior is observed  
 94 for all compositions as well as a change in the magnetic  
 95 anisotropy as a function of *x*. Discussions regarding the advent  
 96 of structural order are also included.

## 97 ■ EXPERIMENTAL SECTION

98 **Synthesis of Yb<sub>0.5</sub>(Co<sub>1-x</sub>Fe<sub>x</sub>)<sub>3</sub>Ge<sub>3</sub>.** Single crystals of  
 99 Yb<sub>0.5</sub>(Co<sub>1-x</sub>Fe<sub>x</sub>)<sub>3</sub>Ge<sub>3</sub> (*x* = 0.00, 0.25, 0.50, 0.75, and 1.00) were  
 100 grown using the flux growth method,<sup>33</sup> using Sn as the low-melting  
 101 metal flux. The elements Yb:Co:Ge:Sn (Yb: 99.9% ingot, Co: 99.95%  
 102 slug, Ge: 99.999% pieces, Sn: 99.99% shot in the ratio of 1.2:6 - *x*:  
 103 6:2:5) with an Fe concentration (Fe: 99.99% pieces) of *x* = 0.00, 1.50,

3.00, 4.50, and 6.00 were weighed out and placed into a Canfield 104  
 alumina crucible set (2 mL container with 13 mm outer diameter)<sup>34</sup> 105  
 with Sn flux above and below the other reactants to ensure 106  
 homogeneity. The container was then sealed inside a fused silica 107  
 tube under ~1/3 atm of Ar gas. These ampules were then heated in a 108  
 programmable furnace from 300 to 1100 °C at a rate of 100 °C/h and 109  
 dwelled at 1100 °C for 24 h. The sample containing ampules were 110  
 then cooled to 900 °C at a rate of 1.5 °C/h. The samples dwelled for 111  
 72 h before they were then removed, inverted, and centrifuged to 112  
 remove excess Sn flux. Excess flux present on the surface of the 113  
 crystals was etched in 1:1 HCl/H<sub>2</sub>O for 1 h. The product of the 114  
 reaction yielded crystals of up to 4 mm with different morphologies 115  
 ranging from needles to plates based on the amount of iron added. 116

The synthesis conditions described above are significantly different 117  
 from the synthesis of the Yb<sub>0.5</sub>Co<sub>3</sub>Ge<sub>3</sub> that we initially reported<sup>27</sup> to 118  
 optimize homogeneous Fe addition across the doped series. A 72 h 119  
 dwell time was performed to ensure that samples were kept consistent 120  
 between batches. The prevalence of the impurity, Fe<sub>2-x</sub>Ge, increases 121  
 as Fe-doping amounts increase. However, Fe<sub>2-x</sub>Ge was mechanically 122  
 separable from the desired product. 123

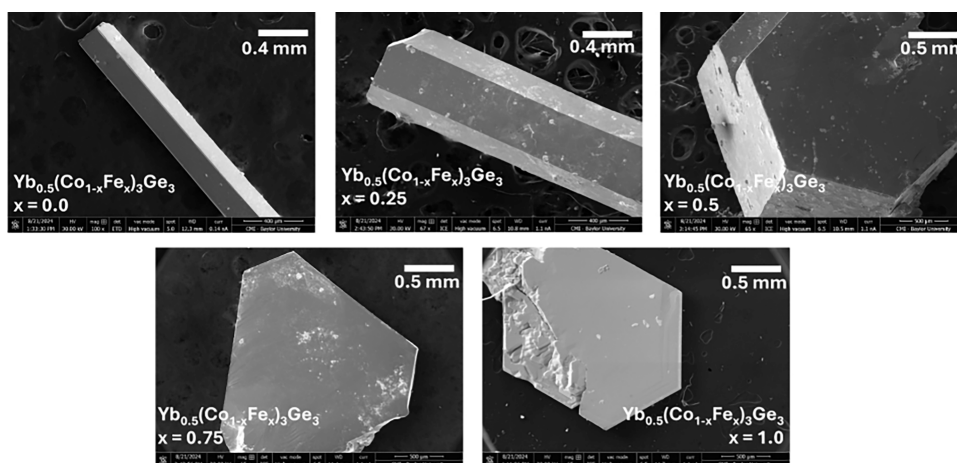
**Structure Determination.** The crystal structures of 124  
 Yb<sub>0.5</sub>(Co<sub>1-x</sub>Fe<sub>x</sub>)<sub>3</sub>Ge<sub>3</sub> (*x* = 0.00, 0.25, 0.50, 0.75, and 1.00) were 125  
 determined using powder X-ray diffraction and single crystal X-ray 126  
 diffraction (SCXRD). Powder X-ray diffraction data (Figures S1 and 127  
 S2) were collected with a Bruker D2 Phaser (Cu Kα radiation, λ = 128  
 1.54184 Å). Single crystal data were collected using a Bruker D8 129  
 Quest Kappa single-crystal X-ray diffractometer with an IμS 130  
 microfocus source (Mo Kα radiation, λ = 0.71073 Å) and a 131  
 PHOTON III CPAD area detector. The raw data frames were 132  
 integrated using the Bruker SAINT program, and a multiscan 133  
 absorption correction was applied using SADABS.<sup>35</sup> Preliminary 134  
 starting models were obtained with the intrinsic phasing method in 135  
 SHELXT for compositions *x* = 0.00, 0.25, 0.75, and 1.00 and a direct 136  
 method in SHELXS for *x* = 0.50 followed by refinement in 137  
 SHELXL.<sup>36</sup> Crystallographic data and refinement parameters of 138  
 each composition are listed in Table S1. Transition metal content was 139  
 constrained to the values obtained from energy-dispersive spectroscopy. 140  
 141

Energy-dispersive (X-ray) spectroscopy (EDS) was performed on 142  
 single crystals of Yb<sub>0.5</sub>(Co<sub>1-x</sub>Fe<sub>x</sub>)<sub>3</sub>Ge<sub>3</sub> (*x* = 0.00, 0.25, 0.50, 0.75, and 143  
 1.00) with a VERSA 3D focused ion beam scanning electron 144

Table 1. Compositions of  $\text{Yb}_{0.5}(\text{Co}_{1-x}\text{Fe}_x)_3\text{Ge}_3$ \* as Obtained from SCXRD and EDS Compared to the Nominal Composition

composition ( $x_{\text{Fe}}$ )	SCXRD	SEM-EDS
Y-Type/CoSn-Type		
0.00	$\text{Yb}_{0.34}\text{Co}_3\text{Ge}_{2.78}\text{Sn}_{0.22}$	$\text{Yb}_{0.433(3)}\text{Co}_{3.000(2)}\text{Ge}_{2.513(2)}\text{Sn}_{0.268(5)}$
0.25	$\text{Yb}_{0.43}\text{Co}_{2.23}\text{Fe}_{0.77}\text{Ge}_{2.85}\text{Sn}_{0.15}$	$\text{Yb}_{0.448(2)}\text{Co}_{2.23(1)}\text{Fe}_{0.77(1)}\text{Ge}_{2.629(8)}\text{Sn}_{0.206(3)}$
H-Type		
0.50	$\text{Yb}_{0.90}\text{Co}_{3.17}\text{Fe}_{2.83}\text{Ge}_{5.80}\text{Sn}_{0.20}$	$\text{Yb}_{0.845(4)}\text{Co}_{3.16(4)}\text{Fe}_{2.83(4)}\text{Ge}_{5.25(3)}\text{Sn}_{0.54(2)}$
0.75	$\text{Yb}_{0.93}\text{Co}_{1.54}\text{Fe}_{4.46}\text{Ge}_{5.85}\text{Sn}_{0.15}$	$\text{Yb}_{0.888(2)}\text{Co}_{1.54(1)}\text{Fe}_{4.455(7)}\text{Ge}_{5.41(2)}\text{Sn}_{0.271(9)}$
1.00	$\text{Yb}_1\text{Fe}_6\text{Ge}_{5.82}\text{Sn}_{0.18}$	$\text{Yb}_{0.929(4)}\text{Fe}_{6.00(1)}\text{Ge}_{5.40(1)}\text{Sn}_{0.176(4)}$

\*For  $x_{\text{Fe}} = 0.50, 0.75,$  and  $1.00$ , the empirical formula was normalized to the “1-6-6” phase instead of the “0.5-3-3” phase.

Figure 2. Images of single crystals of  $\text{Yb}_{0.5}(\text{Co}_{1-x}\text{Fe}_x)_3\text{Ge}_3$  acquired from the SEM. Note the change in morphology from rods to plates with an increasing concentration of Fe.

microscope. An acceleration voltage of 20 kV and a spot size of 6.5 was used to collect data from five spots on each crystal. The compositions are given in Table 1 with a comparison to refined compositions obtained from SCXRD. Images of single crystals obtained from the SEM are shown in Figure 2; the crystal morphology changes from needles to plates as Fe is added. Tiny amounts of Sn are observed in the EDS data for these crystals that were grown out of Sn flux. The small amount is possibly from Sn substitution on Ge sites in the structure. We modeled for Sn in the most probable sites of incorporation across the doped series.<sup>37,38</sup>

**Magnetic Properties.** Measurements of temperature-dependent magnetic susceptibility ( $\chi(T)$ ) and isothermal field-dependent magnetization ( $M(H)$ ) were obtained on single crystals using a VSM SQUID magnetometer from Quantum Design, Model MPMS-3.  $\chi(T)$  was measured from 1.8 to 300 K under an applied field of  $H = 0.1$  T parallel and perpendicular to the  $c$ -axis. The field-dependent measurements were taken at 1.8 K from  $-7$  to 7 T parallel and perpendicular to the  $c$ -axis.

**Resistivity.** Temperature-dependent electrical resistivity ( $\rho(T)$ ) was measured using a physical property measurement system (PPMS) from Quantum Design, model 6000 in the temperature range 1.8–300 K. Four Pt leads were mounted onto the polished single crystals by using silver paste. All samples had varying morphologies, thus the electrical current flowed parallel to the  $c$ -axis in  $x = 0.00$  and 0.25 (rod-shaped crystals), and perpendicular to the  $c$ -axis in  $x = 0.50, 0.75, 1.00$  (plate-shaped crystals).

## RESULTS

**Crystal Structure.** Figure 3 illustrates the relationship among the CoSn,  $\text{HfFe}_6\text{Ge}_6$  (H-type), and  $\text{Y}_{0.5}\text{Co}_3\text{Ge}_3$  (Y-type), structures. The H-type and Y-type structures are regarded as “stuffed variants” of the CoSn structure type.<sup>39</sup> Large electropositive elements insert in-plane into the center of the Ge1 hexagons of the honeycomb net and push out-of-plane

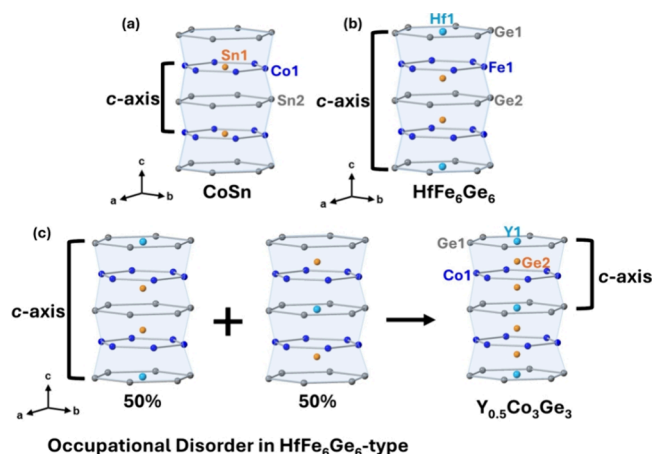
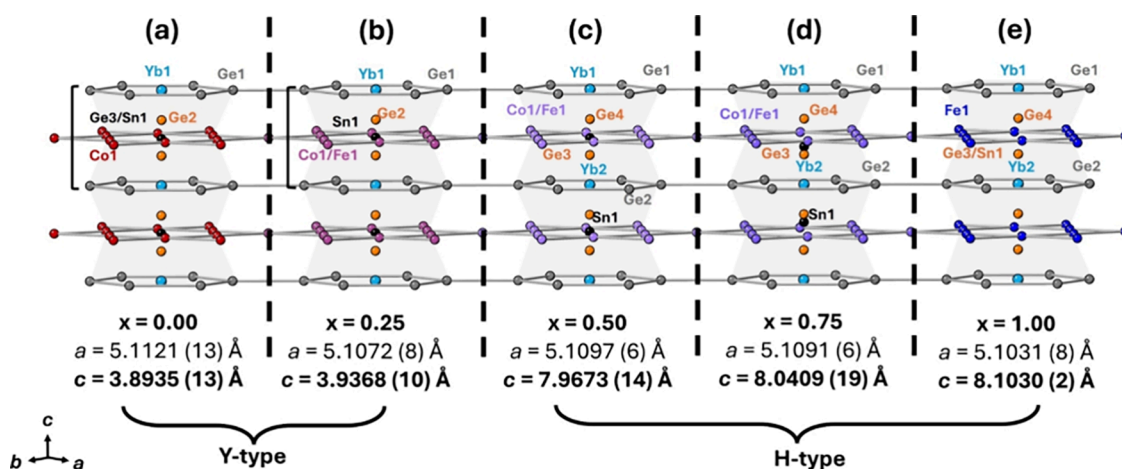


Figure 3. Staggered hexagonal channel motifs of the (a) CoSn, (b)  $\text{HfFe}_6\text{Ge}_6$  (H-type), and (c)  $\text{Y}_{0.5}\text{Co}_3\text{Ge}_3$  (Y-type) structure types, with selected bonds omitted. The relative  $c$ -axis length is emphasized in each of the structure types. (c) The  $\text{Y}_{0.5}\text{Co}_3\text{Ge}_3$  structure type is made up of two H-type unit cells that are occupationally disordered with respect to one another.

the main group element initially centering the kagome net of the CoSn structure type through chemical pressure. All three structures consist of alternating (main group element) honeycomb and (transition metal) kagome slabs. The H-type structure represents the complete ordering of the electropositive and main group element dimers along the  $[001]$  direction. The random positional occupancy of the H-type structure averages 50% each, leading to the Y-type structure. This results in the reduction of the  $c$ -axis length of the unit cell



**Figure 4.** Crystal structures ((a)  $x = 0.00$ , (b)  $x = 0.25$ , (c)  $x = 0.50$ , (d)  $x = 0.75$ , and (e)  $x = 1.00$ ) obtained from single crystal X-ray diffraction, highlighting only the staggered hexagonal channel. All structures have the same space group:  $P6/mmm$  and selected bonds are omitted. The brackets on the left of  $x = 0.00$  and  $0.25$  indicate the  $c$ -axis length and the  $c$ -axis lengths beneath the structures are bolded. Structural information and representations are contained within the Supporting Information (Tables S1–S6 and Figures S3–S7).

187 by half and partial occupancy of the Y1 and Ge2 atoms. The  
 188 Co end member of the  $\text{Yb}_{0.5}(\text{Co}_{1-x}\text{Fe}_x)_3\text{Ge}_3$  series ( $x = 0.00$ )  
 189 possesses a hybrid crystal structure of the Y-type and CoSn  
 190 structure types,<sup>27</sup> while the Fe end member ( $x = 1.00$ )  
 191 adopts the H-type.<sup>22</sup> As Fe is added in this hybrid system, the  
 192 compositions  $x = 0.50$  and  $0.75$  adopt a more ordered  
 193 structure resembling the H-type variant. However, for  
 194 simplicity, the formula  $\text{Yb}_{0.5}(\text{Co}_{1-x}\text{Fe}_x)_3\text{Ge}_3$  will be used with  
 195  $x = 0.00, 0.25, 0.50, 0.75, 1.00$  to describe each member of the  
 196 doped series.

197 **Figure 4** depicts the crystal structures of  
 198  $\text{Yb}_{0.5}(\text{Co}_{1-x}\text{Fe}_x)_3\text{Ge}_3$ . For simplicity, the staggered hexagonal  
 199 channel is highlighted to compare how the site positions differ  
 200 with the Fe addition. The nominal formula used in this article  
 201 does not reflect the small amount of Sn substitution present;  
 202 therefore, **Table 1** provides the nominal concentrations  
 203 compared to the formulas obtained from SCXRD and EDS.  
 204 The complete structural information and representations are  
 205 contained within the Supporting Information (Tables S1–S6  
 206 and Figures S3–S7). The partial occupancy of the atomic sites  
 207 corresponds to the partial occupancy of the structural types  
 208 present.

209 In  $x = 0.00$  (**Figure 4a**), the hybrid  $\text{Y}_{0.5}\text{Co}_3\text{Ge}_3$ –CoSn  
 210 structure type is present and the CoSn-type site is present with  
 211 a higher probability than what was previously reported with  
 212 nearly 31% occupancy. The differences in Yb occupancy are  
 213 attributed to differences in synthesis conditions (reaction ratio  
 214 of elements and temperature profile), the relative Yb content in  
 215 this article is lower than what we previously reported.<sup>27,28</sup> Our  
 216 report of  $\text{Gd}_x\text{Co}_3(\text{Ge}, \text{Sn})_3$  also had a reduced Gd occupancy  
 217 and was grown from a Gd:Co:Ge:Sn 1–6–6–20 ratio.<sup>37</sup> We  
 218 surmise that with increasing the relative Yb ratio in the growth,  
 219 a corresponding increase in Yb occupancy will occur.  $x = 0.25$   
 220 (**Figure 4b**) has a structure similar to that of  $x = 0.00$ , but the  
 221 occupancy of the distinct structure types differs. The CoSn  
 222 structure type is  $\sim 15\%$  in this case. As more Fe is added, the  
 223 structure begins to deviate from the Y-type unit cell; the unit  
 224 cell of  $x = 0.50$  doubles along the  $c$ -axis, resembling the H-type  
 225 structure. As shown in **Figure 3**, the  $\text{Y}_{0.5}\text{Co}_3\text{Ge}_3$  (Y-type)  
 226 structure can be described as disordered  $\text{HfFe}_6\text{Ge}_6$  (H-type),  
 227 exhibiting a 50% occupancy of the H-type positions. The  $x =$   
 228  $0.50$  phase (**Figure 4c**) marks the first composition to display a

229 difference in occupancy of this motif and thus causes the unit  
 230 cell size to double. In addition, the  $1b$  ( $6/mmm$ ) Ge site (Ge3)  
 231 present in  $x = 0.00$ , and  $0.25$  is displaced from the kagome  
 232 plane in  $x = 0.50$  (Sn1), resulting in its site symmetry being  
 233 reduced ( $2e$ ,  $6mm$ ). The  $x = 0.50$  structure contains a rough  
 234 model due to issues with indexing, which we analyze further in  
 235 the **Discussion** section. The  $x = 0.75$  phase (**Figure 4d**) also  
 236 adopts a unit cell similar to the  $\text{HfFe}_6\text{Ge}_6$ -type and has  
 237 differing occupancy of its motifs than  $x = 0.50$ . The Sn1 site  
 238 still retains  $6mm$  symmetry and exhibits a greater displacement  
 239 from the Kagome plane than  $x = 0.50$ . The  $x = 1.00$  phase  
 240 adopts the most ordered  $\text{HfFe}_6\text{Ge}_6$ -type cell when compared  
 241 with the other compositions. There no longer exists an  
 242 additional site that resembles the CoSn structure type,  
 243 implying that the existence of Co influences the presence of  
 244 a CoSn hybrid structure type.

245 A plot of cell dimensions as a function of Fe concentration is  
 246 shown in **Figure 5**. The H-type structures ( $x = 0.50, 0.75, 1.00$ )  
 247 were halved along the  $c$ -axis for easy comparison with the Y-  
 248 type structures ( $x = 0.00, 0.25$ ). As Fe is added, the  $c$ -axis  
 249 length is increased while the  $a$ -axis length stays relatively  
 250 constant.

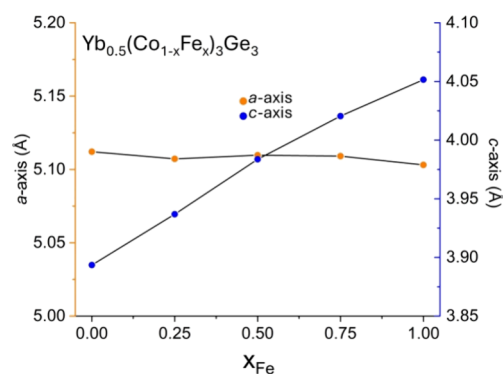


**Figure 5.** Cell dimensions as a function of Fe concentration in  $\text{Yb}_{0.5}(\text{Co}_{1-x}\text{Fe}_x)_3\text{Ge}_3$  by using lattice constants from single crystal X-ray diffraction. The  $c$ -axis length was halved for  $x = 0.50, 0.75$ , and  $1.00$  for comparison across all compounds.

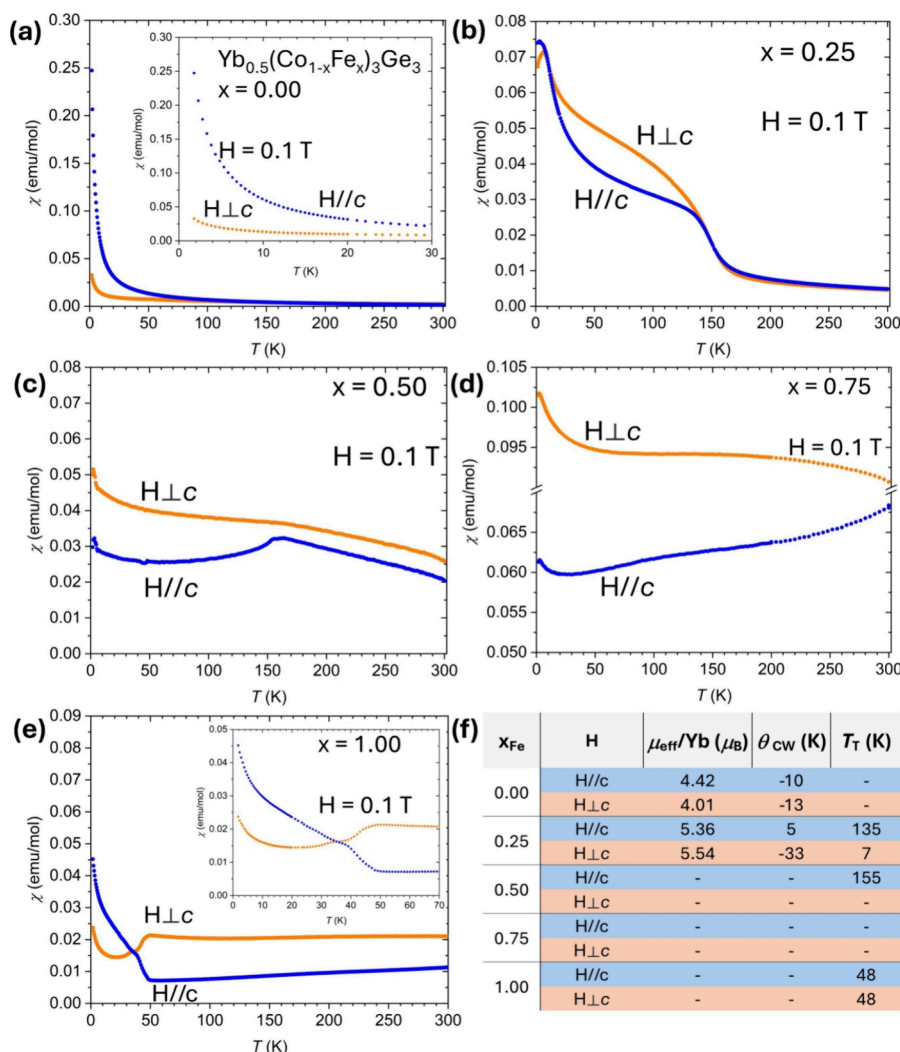


**Figure 6.** (a–e) Anisotropic temperature-dependent magnetometry measurements (H // c in blue and H ⊥ c in orange). Insets are magnifications of the low temperature data. (f) Observed magnetic moment per Yb ( $\mu_{\text{eff}}/\text{Yb}$ ), Curie–Weiss temperature ( $\theta$ ), and observed magnetic transition temperatures ( $T_{\text{T}}$ ). Dashes indicate that values were unobtainable or no transitions were present in the data.

251 **Magnetic Properties.** To evaluate how the magnetic  
 252 properties of  $\text{Yb}_{0.5}(\text{Co}_{1-x}\text{Fe}_x)_3\text{Ge}_3$  change as a function of Fe  
 253 addition, anisotropic temperature-dependent magnetic sus-  
 254 ceptibility measurements were performed, shown in Figure 6.  
 255 The zero-field-cooled (ZFC) data set is reported here as there  
 256 were no extreme differences between the ZFC and the field-  
 257 cooled (FC) data. The isothermal field-dependent magnet-  
 258 ization of each composition is given in Figure 7. Correspond-  
 259 ing Curie–Weiss fits are given in the Supporting Information  
 260 (Figures S8 and S9).

261  $x = 0.00$ . The Co endmember in this series has been  
 262 previously reported to have paramagnetic behavior with an  
 263 effective magnetic moment of  $4.23 \mu_{\text{B}}$ ,<sup>27</sup> lower than the  
 264 calculated  $\text{Yb}^{3+}$  moment of  $\mu_{\text{eff}} = 4.54 \mu_{\text{B}}$ . In this work, the  
 265 effective magnetic moment obtained from the Curie–Weiss fit  
 266 of H // c is  $4.42 \mu_{\text{B}}$ , and that of H ⊥ c is  $4.01 \mu_{\text{B}}$ , and the Weiss  
 267 constants are  $-10$  and  $-13$  K, respectively. The respective  
 268 values agree with previous reports, and the moment obtained  
 269 from the H ⊥ c data is reduced. The isothermal magnetization  
 270 begins to saturate around  $0.7 \mu_{\text{B}}$ , which is similar in magnitude  
 271 to what we previously reported ( $\sim 1 \mu_{\text{B}}$ ).<sup>27</sup> It is possible that  
 272 the reduction of Yb occupancy in the present compound is a  
 273 determining factor in the field-dependent magnetization.

$x = 0.25$ . The effective magnetic moments obtained from 274  
 Curie–Weiss fits from 250 to 300 K are  $5.36$  and  $5.54 \mu_{\text{B}}$  for H 275  
 // c and H ⊥ c, respectively. The elevated magnetic moment 276  
 coupled with the ferromagnetic-like transition  $\sim 135$  K of the H 277  
 // c data indicates that as Fe is added into the kagome net, it 278  
 begins to interact between slabs along the c-axis, and slight 279  
 magnetic ordering is observed. The true magnetic moment of 280  
 the Fe present could not be determined, as a rough Curie– 281  
 Weiss fit was used. There also exists a Néel temperature at 282  
 around 7 K in the H ⊥ c data. The isothermal magnetization 283  
 shows a decrease in the magnitude of the H // c data 284  
 compared to the  $x = 0.00$  composition but still shows that the 285  
 c-axis remains the easy axis with increasing field strength. 286

$x = 0.50$ . A Néel temperature around 155 K is present, near 287  
 where the Curie-like transition existed in  $x = 0.25$ . In addition, 288  
 the H ⊥ c data have an increased magnitude of magnetization 289  
 with no clear magnetic phase transitions. The isothermal 290  
 magnetization shows slight hysteresis in both H ⊥ c, and H // 291  
 c, while no hysteresis is observed in any of the other doped 292  
 concentrations. Additionally, the H ⊥ c data show a higher 293  
 magnetization with increasing field strength. 294

$x = 0.75$ . No magnetic transitions are observed from 2 to 295  
 300 K; however, there is an enhanced magnitude of 296

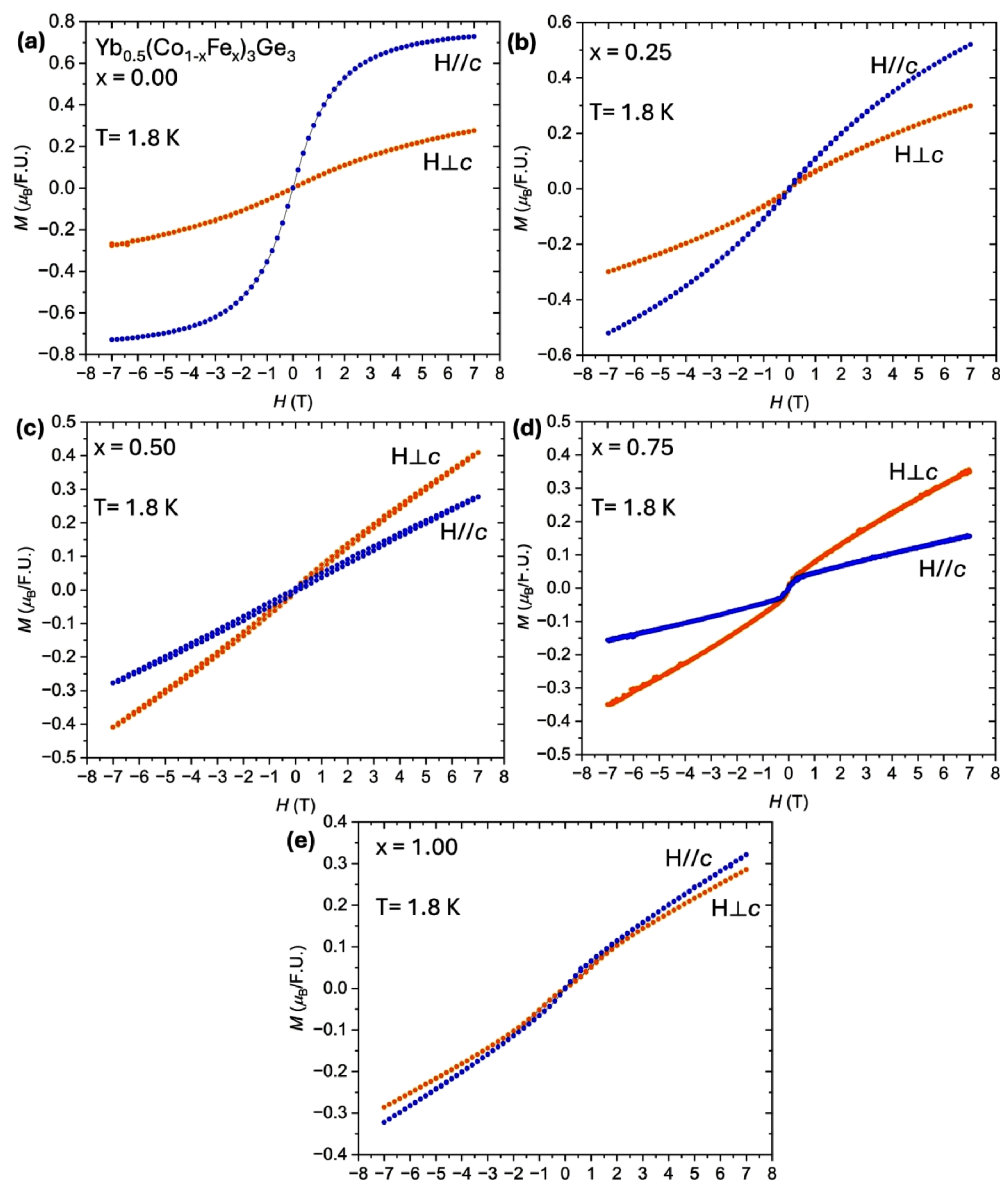


**Figure 7.** (a–e) Isothermal field-dependent magnetization of  $\text{Yb}_{0.5}(\text{Co}_{1-x}\text{Fe}_x)_3\text{Ge}_3$  ( $x = 0.00, 0.25, 0.50, 0.75,$  and  $1.00$ ) measured at 1.8 K.

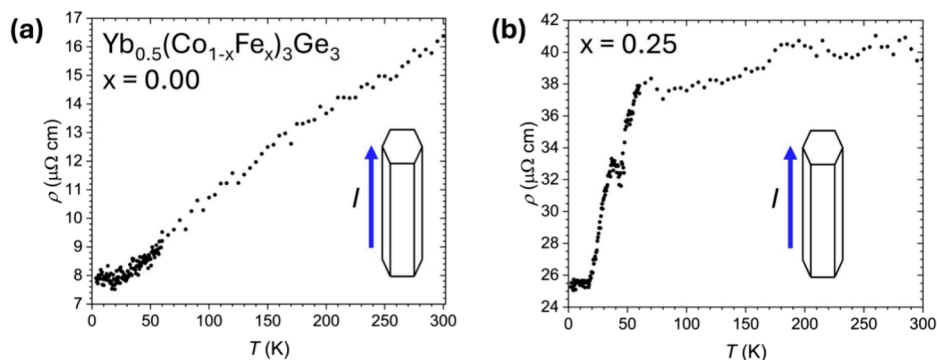


**Figure 8.** (a, b) Temperature dependent resistivity,  $\rho$ , of  $x = 0.00$  and  $0.25$ . The hexagonal 3D shapes represent the morphology of the samples, with the blue arrow representing the direction of the applied current. For (a) and (b), this is parallel to the  $c$ -axis.

297 magnetization of the  $H \perp c$  compared to  $H//c$ . In addition,  
 298 there is an upturn in the  $H//c$  data near 300 K. In the  
 299 isothermal magnetization, the difference in magnitude of the  $H$   
 300  $// c$  and  $H \perp c$  data is much larger than  $x = 0.50$ .

$x = 1.00$ . The Fe end member of the series displays similar  
 301 behavior to what was previously reported by Avila et al.<sup>31</sup> In  
 302 the previous report, a spin reorientation at 63 K was observed,  
 303 resulting in easy-axis inversion from the  $ab$  plane to the  $c$ -axis,  
 304 and could not be detected in the polycrystalline measurements. 305

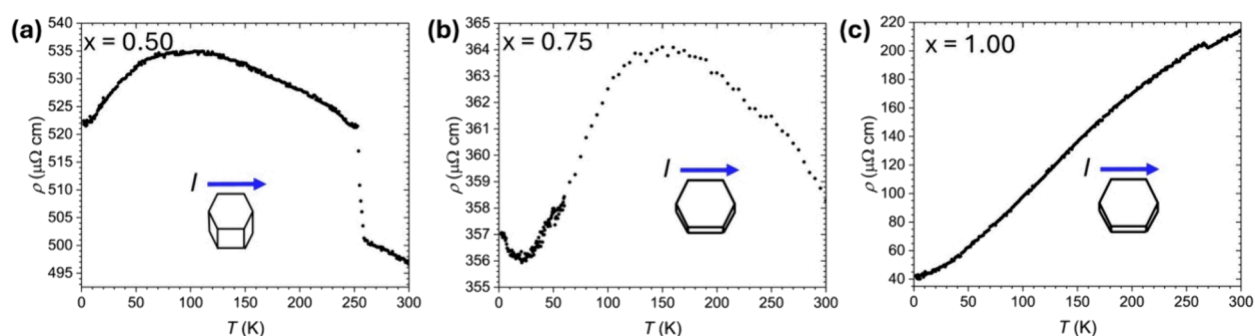


**Figure 9.** (a–c) Temperature-dependent resistivity,  $\rho$ , of  $x = 0.50$ ,  $0.75$ , and  $1.00$ . The hexagonal 3D shapes represent the morphology of the samples with the blue arrow representing the direction of the applied current. For (a–c), the current is applied parallel to the  $ab$  plane.

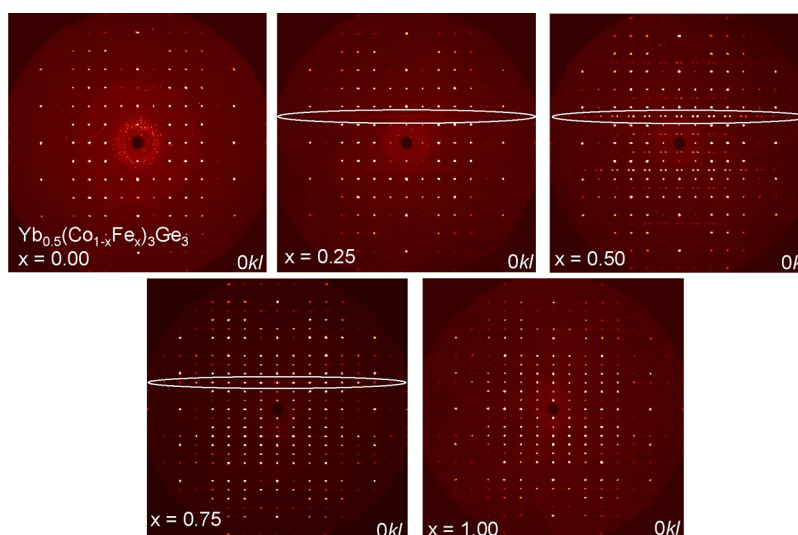


**Figure 10.** (a)  $0kl$  diffraction patterns for  $\text{Yb}_{0.5}(\text{Co}_{1-x}\text{Fe}_x)_3\text{Ge}_3$  ( $x = 0.00, 0.25, 0.50, 0.75$ , and  $1.00$ ) obtained from single crystal X-ray diffraction data. A circled area is shown on  $x = 0.00, 0.25, 0.50, 0.75$ , and  $1.00$  on the  $(0k1.5)$  set of planes for  $x = 0.00, 0.25$ , and  $(0k3)$  set of planes for  $x = 0.50, 0.75$ , and  $1.00$  to emphasize either the diffuse scattering or the broad satellite peaks.

306 Here, the spin reorientation is observed at  $\sim 50$  K with the  
 307 same anisotropy. Additionally, the temperature-dependent  
 308 magnetization below the spin reorientation seems to increase  
 309 drastically in  $H // c$  instead of the saturation previously  
 310 observed. The isothermal magnetization shows similar  
 311 magnitudes along both directions at 1.8 K.

312 **Resistivity.** The resistivity,  $\rho$ , for the Co end member,  $x =$   
 313  $0.00$ , as a function of  $T$  decreases linearly down to low  
 314 temperatures with no observed transition exhibiting simple  
 315 metallic behavior (Figure 8a) in agreement with previous  
 316 reports.<sup>27</sup> The slight increase in the resistivity at 5 K and the  
 317 kink at 95 K of previously reported  $\text{Yb}_{0.5}\text{Co}_3\text{Ge}_3$  is not seen  
 318 here and likely originates from the different amounts of  
 319 occupational disorder or hybridization of the two structure  
 320 types ( $\text{Y}_{0.5}\text{Co}_3\text{Ge}_3$  and  $\text{CoSn}$ ).<sup>27,28</sup> Least-squares fitting of  
 321 resistivity with  $\rho - \rho_0 \propto T^n$  in  $3.5 \text{ K} < T < 40 \text{ K}$  gave  $n = 3.6 \pm$   
 322  $1.1$ , and fitting of up to 50 K gave  $n = 2.4 \pm 0.4$ .<sup>40</sup> These  $n$   
 323 values suggest that other scattering mechanisms besides  
 324 noninteracting electron–electron scattering ( $n = 2$ ) are  
 325 present, such as electron–phonon scattering and electron–  
 326 impurity scattering.<sup>41</sup> Electron–magnetic impurity (Kondo)  
 327 scattering and weak localization effects have been proposed to  
 328 influence the low-temperature resistivity data, but neither has  
 329 been ruled out. Due to the intrinsic amount of structural  
 330 disorder, the values of  $n$  have relatively large errors, but the

trend of increasing  $n$  with lower temperature ranges persists. In  
 331  $x = 0.25$ , the resistivity drastically drops at  $\sim 60$  K (Figure 8b),  
 332 followed by another anomaly at  $\sim 45$  K after which it smooths  
 333 at 17 K. Satisfactory fits of  $\rho - \rho_0 \propto T^n$  could not be obtained  
 334 for  $x = 0.25$ .  
 335

336 Starting with  $x = 0.50$ , in Figure 9a–c, the crystal  
 337 morphology switches from rod-shaped to plate-shaped, which  
 338 coincides with a change in the direction of the applied current  
 339 (from parallel to  $c$ -axis to parallel to the  $ab$  plane). For  $x =$   
 340  $0.50$ , there is a drastic increase in the resistivity of around 259  
 341 K (Figure 9a) with a broad maximum at  $\sim 100$  K.<sup>42</sup> The  
 342 resistivity for  $x = 0.75$  (Figure 9b) shows a broad maximum at  
 343  $\sim 150$  K, then drops sharply below this temperature, and begins  
 344 to saturate as the temperature decreases. The resistivity of the  
 345 Fe-end member,  $x = 1.00$ , (Figure 9c) is in general agreement  
 346 with previous reports, albeit the high-temperature anomaly  
 347 reported herein at  $\sim 250$  K was previously not observed.<sup>31</sup>  
 348 Power-law fits ranging from 2 to 30, 40, and 50 K gave values  
 349 of  $n = 1.4 \pm 0.2, 1.5 \pm 0.1, \text{ and } 1.6 \pm 0.07$ , respectively. This  
 350 agrees with a decrease in electron–phonon scattering, as lower  
 351 temperature ranges are fit. While  $x = 0.00, 0.25, 0.75$ , and  $1.00$   
 352 all see an overall decrease in resistivity as temperature  
 353 decreases, for  $x = 0.50$ , there is a net increase.

## 354 ■ DISCUSSION

355 **Structural Evolution.** When viewing the  $0kl$  direction of  
 356 the diffraction pattern for  $\text{Yb}_{0.5}(\text{Co}_{1-x}\text{Fe}_x)_3\text{Ge}_3$  ( $x = 0.00, 0.25,$   
 357  $0.50, 0.75, 1.00$ ), either diffuse scattering or broad satellite  
 358 peaks can be seen in most of the doped compositions ( $x =$   
 359  $0.25, 0.50, 0.75$ ), shown in Figures 10 and 11a. When

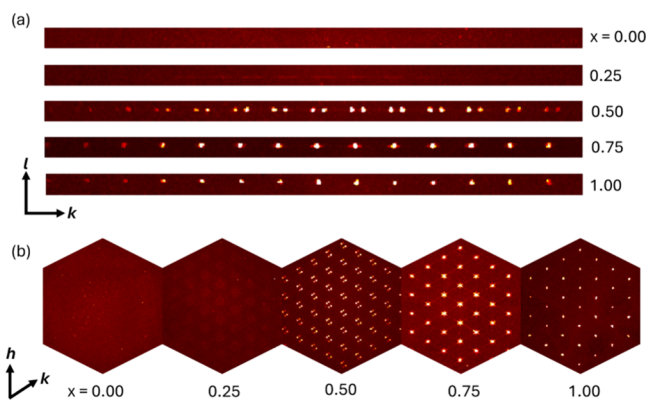


**Figure 11.** (a) Zoomed-in view of the  $0k1.5$  set of planes ( $x = 0.00, 0.25$ ) and on the  $0k3$  set of planes ( $x = 0.50, 0.75, 1.00$ ). (b) Section of the  $hk1.5$  and  $hk3$  views of the reciprocal lattice.

360 examining the  $hk1.5$  ( $x = 0.00, 0.25$ ) and  $hk3$  ( $x = 0.50, 0.75,$   
 361 and  $1.00$ ) sections of the reciprocal lattice, the diffuse  
 362 scattering converges into one reflection as the Fe content  
 363 increases as shown in Figure 11b. Diffuse scattering in the  
 364  $\text{AM}_6\text{X}_6$  family has been observed before with  $M = \text{Co}$ .<sup>43</sup>  
 365 Diffuse scattering occurs when X-rays interact with a material  
 366 that has disorder or irregularity in its crystal structure. Unlike  
 367 Bragg scattering, which results in sharp, well-defined peaks  
 368 corresponding to the average periodic structure of a crystal,  
 369 diffuse scattering appears as a spread-out signal over a range of  
 370 angles and will require pair distribution function analysis  
 371 (PDF) and the usage of synchrotron sources to probe local  
 372 structure.<sup>44–46</sup> The extra reflections in  $x = 0.50$  indicate that a  
 373 larger unit cell or the addition of incommensurate modulation  
 374 vectors is needed, as they are not indexed when using the  
 375 current hexagonal unit cell. Unsuccessful attempts to model  
 376 this composition with an orthorhombic cell were made to  
 377 index the reflections as twin domains. Figures S10 and S11  
 378 show the indexed reflections of  $x = 0.50$  using both the  
 379 hexagonal and orthorhombic cells, respectively. Regarding the  
 380  $hk3$  precession image in Figure 11b for  $x = 0.50$ , there are clear  
 381 complex diffraction features that are not uncommon in

$\text{AFe}_6\text{Sn}_6$  compounds, which may be due to a “twinned  
 382 microstructure”.<sup>47,48</sup> We speculate the diffuse scattering  
 383 observed as well as the unindexable extra reflections present  
 384 in  $x = 0.50$  are caused by incommensurate ordering intrinsic to  
 385 the crystal structure. Although the  $hk3$  reflections were focused  
 386 on for this  $x = 0.50$  discussion, the extra reflections are present  
 387 on other  $l = \text{odd}$  precession planes, except for  $hk7$ .  
 388

The polymorphism and superstructure ordering in the  
 389  $\text{AM}_6\text{X}_6$  family were detailed by Fredrickson et al.<sup>49</sup> It was  
 390 found that  $\text{ScFe}_6\text{Ge}_6$  with the hexagonal  $\text{HfFe}_6\text{Ge}_6$  structure  
 391 type (space group:  $P6/mmm$ ) is dominated by electrostatic  
 392 effects while  $\text{ScFe}_6\text{Ga}_6$  with the orthorhombic  $\text{ScFe}_6\text{Ga}_6$   
 393 structure type (space group:  $Immm$ ) is primarily influenced  
 394 by unfavorable steric interactions. It is the competition of these  
 395 two effects that leads to the structural variety in this family.  
 396 The  $\text{Y}_{0.5}\text{Co}_3\text{Ge}_3$  structure type is an outlier in this family that  
 397 maintains its hexagonal symmetry while bypassing the steric  
 398 obstacles of the large electropositive element. This specific  
 399 polymorphism between orthorhombic superstructures and the  
 400 Y-type is seen with  $\text{AFe}_6\text{Ge}_6$ , with A being the larger  
 401 lanthanides.<sup>50</sup> The isolation of either phase was observed to  
 402 be dependent on synthesis conditions. With this in mind,  
 403 specific interatomic distances were analyzed across this doped  
 404 series. As Fe content increases, the M1–M1 interatomic  
 405 distances that encompass the local environment of the Yb  
 406 increase, as shown in Figure 12. The M1–M1<sub>c-axis</sub> distances  
 407 f12 change significantly relative to the M1–M1<sub>ab-plane</sub> distances,  
 408 showing a similar trend as the lattice parameters in Figure 5.  
 409 The 20-coordinate environment that surrounds Yb becomes  
 410 larger as more Fe is added, allowing for a sterically favored  
 411 configuration, leading to the structural order that arises. The  
 412 majority of studies of structural transitions from the H-type to  
 413 other orthorhombic variants in  $\text{AM}_6\text{X}_6$  vary the X element  
 414 composition through substitution.<sup>39,49,51,52</sup> One example of  
 415 structural deviation with varied transition metal contents is in  
 416  $\text{YbMn}_{6-x}\text{Fe}_x\text{Sn}_6$ . The  $\text{YbMn}_6\text{Sn}_6$  parent compound hosts an  
 417 intermediate valent Yb state and adopts a slightly disordered  
 418 H-type structure.<sup>53,54</sup> As Fe is added into the Mn sublattice,  
 419 the chemical pressure surrounding the Yb atom causes the  
 420 structure to shift to the  $\text{HoFe}_6\text{Sn}_6$ -type, an orthorhombic  
 421 structure type with space group  $Immm$ .<sup>53,54</sup> A summary of this  
 422 concept is shown in Figure S12. As the chemical pressure  
 423 increases around the A site, the A elements form a staggered  
 424 configuration with respect to one another along their  
 425 respective axes. The frequency of this staggering decreases  
 426 from the  $\text{ErFe}_6\text{Sn}_6$ -type, with every four A sites, to the  
 427  $\text{ScFe}_6\text{Ga}_6$  structure, type, the most sterically favored config-  
 428 uration with every other A element being staggered. The  
 429

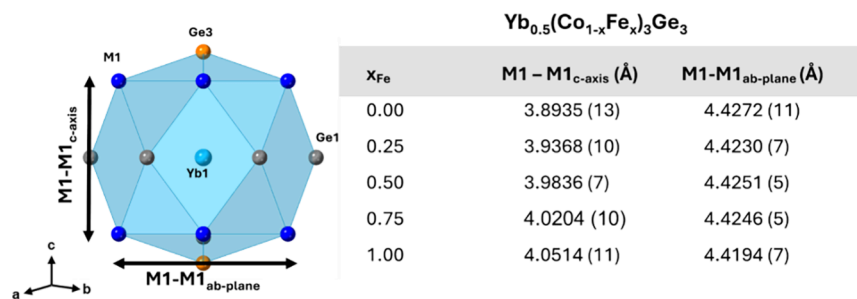


**Figure 12.** Local environment of Yb1 with the M1–M1 ( $M = \text{Co, Fe}$ ) interatomic distances emphasized. The M1–M1 distance along the  $c$ -axis increases as Fe is incorporated, while the M1–M1 distance along the  $ab$  plane remains relatively constant. This increase in the M1–M1<sub>c-axis</sub> causes the interstitial space that the Yb occupies to increase.

430  $\text{Y}_{0.5}\text{Co}_3\text{Ge}_3$  structure type is shown as an alternative way to  
431 crystallize, showing a random ordering of the A element. The  
432 complex ordering of the “166” phases is a possible reason why  
433 the morphology of the disordered members of the  
434  $\text{Yb}_{0.5}(\text{Co}_{1-x}\text{Fe}_x)_3\text{Ge}_3$  series ( $x = 0.00, 0.25$ ) form hexagonal  
435 needles, while the ordered members ( $x = 0.75$  and  $1.00$ ) form  
436 hexagonal plates.  $x = 0.50$  has a hexagonal block shape, which  
437 is an intermediate morphology of the needles and plates. The  
438 ordering of the A element is greatly affected along the same  
439 axes that the alternating layers run parallel to ( $ab$  plane in the  
440 hexagonal H-type structure) in the polymorphs of this  
441 structure. It is plausible that crystallization along the  $ab$   
442 plane is less favorable, resulting in needles for the randomly  
443 disordered structures (Y-type) and more plate-like for the  
444 ordered structures (H-type).

445 **Physical Properties.** Within the temperature-dependent  
446 magnetic data taken from 1.8 to 300 K, magnetic transitions  
447 are present only in  $x = 0.25, 0.50$ , and  $1.00$ . Previously  
448 reported  $\text{ACo}_6\text{Ge}_6$  ( $A = \text{Y, Dy, Er-Lu}$ ) compounds show  
449 paramagnetic behavior from 78 to 293 K and no Co magnetic  
450 contribution in the temperature-dependent magnetic suscepti-  
451 bility.<sup>55</sup> Our prior report of  $\text{Gd}_x\text{Co}_3(\text{Ge,Sn})_3$  did display Co  
452 contribution in the temperature-dependent magnetic data with  
453  $H // a$ .<sup>37</sup> Fe moments within the pure  $\text{AFe}_6\text{Ge}_6$  ( $A = \text{Sc, Y,}$   
454  $\text{Nd, Sm, and Gd-Lu}$ ) have shown to independently and  
455 antiferromagnetically order at temperatures ranging from 400  
456 to 500 K.<sup>22,56</sup> The Yb analog is the only one that has shown  
457 this drastic spin reorientation of the Fe sublattice at low  
458 temperatures and also only occurs in the ordered H-type  
459 polymorph.<sup>32</sup> Through neutron diffraction studies, the Fe  
460 sublattice was determined to order ferromagnetically with  
461 antiferromagnetic order between neighboring Fe slabs in an  
462 axial configuration along the  $c$ -axis.<sup>57-59</sup> We hypothesize that  
463 as Fe is substituted for Co in  $\text{Yb}_{0.5}\text{Co}_3\text{Ge}_3$ , long-range  
464 magnetic ordering is introduced between the kagome layers  
465 in an axial fashion along the  $c$ -axis. In  $x = 0.25$ , the Fe content  
466 is insufficient, causing a low-temperature ferromagnetic-like  
467 transition at  $\sim 135$  K as well as a low-temperature Néel  
468 transition ( $T_N$ ) at 7 K in  $H \perp c$ . The  $T_N$  in the  $H \perp c$  data is  
469 reminiscent of planar antiferromagnetic ordering akin to the  
470 behavior in  $\text{FeSn}$ .<sup>60</sup> As more Fe is added, in  $x = 0.50$ , a clear  
471  $T_N$  is observed at 155 K. The field-dependent data support  
472 how Fe introduces long-range ordering in this system by  
473 showing the change in anisotropy. Increasing the Fe content  
474 promotes interlayer antiferromagnetic ordering along the  $c$ -axis  
475 thus causing the easy axis to invert. The data was collected at  
476 1.8 K, which explains why the trend breaks at  $x = 1.00$ , as the  
477 pure Fe endmember undergoes a spontaneous change in  
478 anisotropy at 48 K, which is unaffected by the strength of the  
479 applied field up to 7 T.

480 The change in magnitudes of the resistivity (Figures 8 and  
481 9) for each compound is in line with the intrinsic disorder  
482 visible in single-crystal X-ray structural models. The residual  
483 resistivities ( $\rho_0$ ) for  $x = 0.00, 0.25, 0.50, 0.75$ , and  $1.00$  are 8,  
484 25, 522, 357, and  $42 \mu\Omega \text{ cm}$ , respectively. High  $\rho_0$  values  
485 usually correspond to high degrees of structural disorder. Here,  
486 we have compounds subjected to not only structural disorder  
487 but also compositional disorder. For  $x = 0.00$  and  $0.25$ , the  
488 resistivity was measured along the  $c$ -axis or along the length of  
489 the needle-shaped crystal, but for  $x = 0.50, 0.75$ , and  $1.00$ , the  
490 resistivity was measured parallel to the  $ab$  plane or  
491 perpendicular to the thickness of the plate-shaped crystal due  
492 to the change in morphology. The lack of direct trends as Co is

substituted for Fe could be due, in part, to the fact that the  
electrical transport for  $x = 0.00$  and  $0.25$  is measured  
perpendicular to the alternating hexagonal and kagome slabs,  
but for  $x = 0.50, 0.75$ , and  $1.00$ , the electrical transport is  
measured parallel to the slabs. We speculate that this results in  
a change of observable electron scattering as temperature is  
decreased.

## CONCLUSIONS

In this article, we report the single crystal growth and X-ray  
diffraction of  $\text{Yb}_{0.5}(\text{Co}_{1-x}\text{Fe}_x)_3\text{Ge}_3$  ( $x = 0.00, 0.25, 0.50, 0.75$ ,  
and  $1.00$ ). The substitution of Fe results in a larger local  
environment around the Yb atoms, subsequently leading to the  
ordered  $\text{HfFe}_6\text{Ge}_6$ -type structure that arises. The diffuse  
scattering in  $x = 0.25, 0.50$ , and  $0.75$  points to the possibility  
that the local symmetry is being altered, which has been  
observed in the closely related  $(\text{Co}_{0.45}\text{Fe}_{0.55})\text{Sn}$ .<sup>61</sup> Endeavors in  
probing the local environments of this material will give way to  
understanding how the change in structure relates to the  
change in the physical properties. The magnetic interactions of  
the  $\text{Yb}_{0.5}(\text{Co}_{1-x}\text{Fe}_x)_3\text{Ge}_3$  doped series appear to predominately  
occur along the  $c$ -axis suggesting that the moments are coupled  
with one another between the layers. Obtaining the magnetic  
structures of these compounds is an avenue for future studies.  
A study recently reported by the Shatruk group explored the  
characteristics of polycrystalline  $\text{YFe}_{6-x}\text{Co}_6\text{Ge}_6$ .<sup>62</sup> A similar  
trend is observed in the magnetic susceptibility, with the  $T_N$   
suppressing to lower temperatures with reduced Fe content.  
Additionally, the density-functional theory (DFT) calculations  
reveal that the increasing Co content leads to the filling of 3d  
states, moving the density of states (DOS) further away from  
the Fermi level, which rationalized the ferromagnetic-like  
behavior observed.

According to the least-squares fitting of the experimental  
resistivity data with  $\rho - \rho_0 \propto T^n$  for  $\text{Yb}_{0.5}(\text{Co}_{1-x}\text{Fe}_x)_3\text{Ge}_3$ , we  
suspect the interplay of multiple scattering mechanisms and  
crystal electric field effects for all members of this series. It is  
clear that as Co becomes increasingly substituted for Fe, the  
electronic structures of these Kagome materials are drastically  
changing, providing a rich platform to study strong  
correlations. Band structure calculations and field-dependent  
and pressure-dependent resistivity measurements will help  
unravel the dominant scattering mechanisms that give rise to  
the seemingly complex electronic structures presented here.

## ASSOCIATED CONTENT

### Supporting Information

The Supporting Information is available free of charge at  
<https://pubs.acs.org/doi/10.1021/acs.chemmater.5c00119>.

(Figures S1 and S2) Powder diffraction patterns of  
 $\text{Yb}_{0.5}(\text{Co}_{1-x}\text{Fe}_x)_3\text{Ge}_3$  ( $x = 0.00, 0.25, 0.50, 0.75$ , and  
 $1.00$ ); (Table S1) crystallographic data and refinement  
parameters; (Figures S3–S7) full unit cells of  
 $\text{Yb}_{0.5}(\text{Co}_{1-x}\text{Fe}_x)_3\text{Ge}_3$  ( $x = 0.00, 0.25, 0.50, 0.75$ , and  
 $1.00$ ); (Tables S2–S6) atomic coordinates and atomic  
displacement parameters; (Figures S8 and S9) Curie–  
Weiss fitted data for  $\text{Yb}_{0.5}(\text{Co}_{1-x}\text{Fe}_x)_3\text{Ge}_3$  ( $x = 0.00$  and  
 $0.25$ ); (Figures S10 and S11) indexed precession images  
of  $\text{Yb}_{0.5}(\text{Co}_{1-x}\text{Fe}_x)_3\text{Ge}_3$  ( $x = 0.50$ ) to highlight the extra  
reflections; (Figure S12) structural comparison of the  
“166” phases (PDF)

552 **Accession Codes**

553 CCDC 2417068 ( $\text{Yb}_{0.34}\text{Co}_3\text{Ge}_{2.78}\text{Sn}_{0.22}$ ), CCDC 2417069  
554 ( $\text{Yb}_{0.43}\text{Co}_{2.23}\text{Fe}_{0.77}\text{Ge}_{2.85}\text{Sn}_{0.15}$ ), CCDC 2417071  
555 ( $\text{Yb}_{0.93}\text{Co}_{1.54}\text{Fe}_{4.46}\text{Ge}_{5.85}\text{Sn}_{0.15}$ ), and CCDC 2417079 ( $\text{Yb}$ -  
556  $\text{Fe}_6\text{Ge}_{5.82}\text{Sn}_{0.18}$ ) contain the supplementary crystallographic  
557 data for this paper. These data can be obtained free of charge  
558 via [www.ccdc.cam.ac.uk/data\\_request/cif](http://www.ccdc.cam.ac.uk/data_request/cif), or by emailing  
559 [data\\_request@ccdc.cam.ac.uk](mailto:data_request@ccdc.cam.ac.uk), or by contacting The Cam-  
560 bridge Crystallographic Data Centre, 12 Union Road,  
561 Cambridge CB2 1EZ, UK; fax: + 44 1223 336033.

562 ■ **AUTHOR INFORMATION**563 **Corresponding Author**

564 **Julia Y. Chan** – Department of Chemistry and Biochemistry,  
565 Baylor University, Waco, Texas 76706, United States;  
566 [orcid.org/0000-0003-4434-2160](https://orcid.org/0000-0003-4434-2160); Email: [Julia\\_Chan@](mailto:Julia_Chan@baylor.edu)  
567 [baylor.edu](mailto:Julia_Chan@baylor.edu)

568 **Authors**

569 **Rahul Meduri** – Department of Chemistry and Biochemistry,  
570 Baylor University, Waco, Texas 76706, United States

571 **Mario A. Plata** – Department of Chemistry and Biochemistry,  
572 Baylor University, Waco, Texas 76706, United States

573 **Gregory T. McCandless** – Department of Chemistry and  
574 Biochemistry, Baylor University, Waco, Texas 76706, United  
575 States

576 **Benny C. Schundelmier** – Department of Physics, Florida  
577 State University, Tallahassee, Florida 32306, United States;  
578 National High Magnetic Field Laboratory, Florida State  
579 University, Tallahassee, Florida 32310, United States;  
580 [orcid.org/0000-0002-7345-9977](https://orcid.org/0000-0002-7345-9977)

581 **Mehak Ghafoor** – Department of Physics, Florida State  
582 University, Tallahassee, Florida 32306, United States;  
583 National High Magnetic Field Laboratory, Florida State  
584 University, Tallahassee, Florida 32310, United States

585 **Kaya Wei** – National High Magnetic Field Laboratory,  
586 Florida State University, Tallahassee, Florida 32310, United  
587 States

588 Complete contact information is available at:

589 <https://pubs.acs.org/10.1021/acs.chemmater.5c00119>

590 **Notes**

591 The authors declare no competing financial interest.

592 ■ **ACKNOWLEDGMENTS**

593 J.Y.C. and R.M. acknowledge DOE: DE-SC0022854 and  
594 Welch: AA-2056-20240404 for support of this work. A portion  
595 of this work was performed at the National High Magnetic  
596 Field Laboratory (NHMFL), which is supported by National  
597 Science Foundation Cooperative Agreement No. DMR-  
598 2128556 and the State of Florida. B.S., M.G., and K.W.  
599 acknowledge the support of the NHMFL User Collaboration  
600 Grant Program (UCGP).

601 ■ **REFERENCES**

602 (1) Wang, Y.; Wu, H.; McCandless, G. T.; Chan, J. Y.; Ali, M. N.  
603 Quantum States and Intertwining Phases in Kagome Materials. *Nat.*  
604 *Rev. Phys.* **2023**, *5*, 635–658.  
605 (2) Jovanovic, M.; Schoop, L. M. Simple Chemical Rules for  
606 Predicting Band Structures of Kagome Materials. *J. Am. Chem. Soc.*  
607 **2022**, *144*, 10978–10991.  
608 (3) Ortiz, B. R.; Gomes, L. C.; Morey, J. R.; Winiarski, M.; Bordelon,  
609 M.; Mangum, J. S.; Oswald, I. W. H.; Rodriguez-Rivera, J. A.; Neilson,

J. R.; Wilson, S. D.; Ertekin, E.; McQueen, T. M.; Toberer, E. S. New  
610 Kagome Prototype Materials: Discovery of  $\text{KV}_3\text{Sb}_5$ ,  $\text{RbV}_3\text{Sb}_5$ , and  
611  $\text{CsV}_3\text{Sb}_5$ . *Phys. Rev. Mater.* **2019**, *3*, No. 094407.

(4) Li, H.; Zhang, T. T.; Yilmaz, T.; Pai, Y. Y.; Marvinney, C. E.;  
613 Said, A.; Yin, Q. W.; Gong, C. S.; Tu, Z. J.; Vescovo, E.; Nelson, C. S.;  
614 Moore, R. G.; Murakami, S.; Lei, H. C.; Lee, H. N.; Lawrie, B. J.;  
615 Miao, H. Observation of Unconventional Charge Density Wave  
616 without Acoustic Phonon Anomaly in Kagome Superconductors  
617  $\text{AV}_3\text{Sb}_5$  (A = Rb, Cs). *Phys. Rev. X* **2021**, *11*, No. 031050.

(5) Ortiz, B. R.; Teicher, S. M. L.; Hu, Y.; Zuo, J. L.; Sarte, P. M.;  
619 Schueller, E. C.; Abeykoon, A. M. M.; Krogstad, M. J.; Rosenkranz, S.;  
620 Osborn, R.; Seshadri, R.; Balents, L.; He, J.; Wilson, S. D.  $\text{CsV}_3\text{Sb}_5$ : A  
621  $\text{Z}_2$  Topological Kagome Metal with a Superconducting Ground State.  
622 *Phys. Rev. Lett.* **2020**, *125*, No. 247002.

(6) Yang, S.-Y.; Wang, Y.; Ortiz, B. R.; Liu, D.; Gayles, J.; Derunova,  
624 E.; Gonzalez-Hernandez, R.; Šmejkal, L.; Chen, Y.; Parkin, S. S. P.;  
625 Wilson, S. D.; Toberer, E. S.; McQueen, T.; Ali, M. N. Giant,  
626 Unconventional Anomalous Hall Effect in the Metallic Frustrated  
627 Magnet Candidate,  $\text{KV}_3\text{Sb}_5$ . *Sci. Adv.* **2020**, *6*, No. eabb6003.

(7) Yu, F. H.; Wu, T.; Wang, Z. Y.; Lei, B.; Zhuo, W. Z.; Ying, J. J.;  
629 Chen, X. H. Concurrence of Anomalous Hall Effect and Charge  
630 Density Wave in a Superconducting Topological Kagome Metal. *Phys.*  
631 *Rev. B* **2021**, *104*, No. L041103.

(8) Ortiz, B. R.; Teicher, S. M. L.; Kautzsch, L.; Sarte, P. M.; Ratcliff,  
633 N.; Harter, J.; Ruff, J. P. C.; Seshadri, R.; Wilson, S. D. Fermi Surface  
634 Mapping and the Nature of Charge-Density-Wave Order in the  
635 Kagome Superconductor  $\text{CsV}_3\text{Sb}_5$ . *Phys. Rev. X* **2021**, *11*, No. 041030.

(9) Kautzsch, L.; Ortiz, B. R.; Mallayya, K.; Plumb, J.; Pokharel, G.;  
637 Ruff, J. P. C.; Islam, Z.; Kim, E.-A.; Seshadri, R.; Wilson, S. D.  
638 Structural Evolution of the Kagome Superconductors  $\text{AV}_3\text{Sb}_5$  (A = K,  
639 Rb, and Cs) Through Charge Density Wave Order. *Phys. Rev. Mater.*  
640 **2023**, *7*, No. 024806.

(10) Teng, X.; Chen, L.; Ye, F.; Rosenberg, E.; Liu, Z.; Yin, J.-X.;  
642 Jiang, Y.-X.; Oh, J. S.; Hasan, M. Z.; Neubauer, K. J.; Gao, B.; Xie, Y.;  
643 Hashimoto, M.; Lu, D.; Jozwiak, C.; Bostwick, A.; Rotenberg, E.;  
644 Birgeneau, R. J.; Chu, J.-H.; Yi, M.; Dai, P. Discovery of Charge  
645 Density Wave in a Kagome Lattice Antiferromagnet. *Nature* **2022**,  
646 609, 490–495.

(11) Shao, S.; Yin, J.-X.; Belopolski, I.; You, J.-Y.; Hou, T.; Chen, H.;  
648 Jiang, Y.; Hossain, M. S.; Yahyavi, M.; Hsu, C.-H.; Feng, Y. P.; Bansil,  
649 A.; Hasan, M. Z.; Chang, G. Intertwining of Magnetism and Charge  
650 Ordering in Kagome  $\text{FeGe}$ . *ACS Nano* **2023**, *17*, 10164–10171.

(12) Wu, X.; Mi, X.; Zhang, L.; Wang, C.-W.; Maraytta, N.; Zhou,  
652 X.; He, M.; Merz, M.; Chai, Y.; Wang, A. Annealing-Tunable Charge  
653 Density Wave in the Magnetic Kagome Material  $\text{FeGe}$ . *Phys. Rev. Lett.*  
654 **2024**, *132*, No. 256501.

(13) Hou, Z.; Ren, W.; Ding, B.; Xu, G.; Wang, Y.; Yang, B.; Zhang,  
656 Q.; Zhang, Y.; Liu, E.; Xu, F.; Wang, W.; Wu, G.; Zhang, X.; Shen, B.;  
657 Zhang, Z. Observation of Various and Spontaneous Magnetic  
658 Skyrmionic Bubbles at Room Temperature in a Frustrated Kagome  
659 Magnet with Uniaxial Magnetic Anisotropy. *Adv. Mater.* **2017**, *29*,  
660 No. 1701144.

(14) Kida, T.; Fenner, L. A.; Dee, A. A.; Terasaki, I.; Hagiwara, M.;  
662 Wills, A. S. The Giant Anomalous Hall Effect in the Ferromagnet  
663  $\text{Fe}_3\text{Sn}_2$ —a Frustrated Kagome Metal. *J. Phys.: Condens. Matter* **2011**,  
664 *23*, No. 112205.

(15) Natarajan, S.; Rao, G. V. S.; Baskaran, R.; Radhakrishnan, T. S.  
666 Synthesis and Electrical Properties of Shandite-Parkerite Phases,  
667  $\text{A}_2\text{M}_3\text{Ch}_2$ . *J. Less-Common Met.* **1988**, *138*, 215–224.

(16) Vaquero, P.; Sobany, G. G. A Powder Neutron Diffraction  
669 Study of the Metallic Ferromagnet  $\text{Co}_3\text{Sn}_2\text{S}_2$ . *Solid. State. Sci.* **2009**,  
670 *11*, 513–518.

(17) Wang, Q.; Xu, Y.; Lou, R.; Liu, Z.; Li, M.; Huang, Y.; Shen, D.;  
672 Weng, H.; Wang, S.; Lei, H. Large Intrinsic Anomalous Hall Effect in  
673 Half-Metallic Ferromagnet  $\text{Co}_3\text{Sn}_2\text{S}_2$  with Magnetic Weyl Fermions.  
674 *Nat. Commun.* **2018**, *9*, 3681.

(18) Xu, X.; Yin, J.-X.; Qu, Z.; Jia, S. Quantum Interactions in  
676 Topological  $\text{Rl}66$  Kagome Magnet. *Rep. Prog. Phys.* **2023**, *86*,  
677 No. 114502.

- 679 (19) Arachchige, H. W. S.; Meier, W. R.; Marshall, M.; Matsuoka, T.; Xue, R.; McGuire, M. A.; Hermann, R. P.; Cao, H.; Mandrus, D. Charge Density Wave in Kagome Lattice Intermetallic  $\text{ScV}_6\text{Sn}_6$ . *Phys. Rev. Lett.* **2022**, *129*, No. 216402.
- 683 (20) Ortiz, B. R.; Meier, W. R.; Pokharel, G.; Chamorro, J.; Yang, F.; Mozaffari, S.; Thaler, A.; Gomez Alvarado, S. J.; Zhang, H.; Parker, D. S.; Samolyuk, G. D.; Paddison, J. A. M.; Yan, J.; Ye, F.; Sarker, S.; Wilson, S. D.; Miao, H.; Mandrus, D.; McGuire, M. A. Stability Frontiers in the  $\text{AM}_6\text{X}_6$  Kagome Metals: The  $\text{LnNb}_6\text{Sn}_6$  ( $\text{Ln}:\text{Ce}-\text{Lu}, \text{Y}$ ) Family and Density-Wave Transition in  $\text{LuNb}_6\text{Sn}_6$ . *J. Am. Chem. Soc.* **2025**, *147*, 5279–5292.
- 690 (21) Meier, W. R.; Madhogaria, R. P.; Mozaffari, S.; Marshall, M.; Graf, D. E.; McGuire, M. A.; Arachchige, H. W. S.; Allen, C. L.; Driver, J.; Cao, H.; Mandrus, D. Tiny Sc Allows the Chains to Rattle: Impact of Lu and Y Doping on the Charge-Density Wave in  $\text{ScV}_6\text{Sn}_6$ . *J. Am. Chem. Soc.* **2023**, *145*, 20943–20950.
- 695 (22) Venturini, G.; Welter, R.; Malaman, B. Crystallographic Data and Magnetic Properties of  $\text{RT}_6\text{Ge}_6$  compounds ( $\text{R} = \text{Sc}, \text{Y}, \text{Nd}, \text{Sm}, \text{Gd}-\text{Lu}; \text{T} = \text{Mn}, \text{Fe}$ ). *J. Alloys Compd.* **1992**, *185*, 99–107.
- 698 (23) Malaman, B.; Venturini, G.; Roques, B. Nouveaux Stannures Ternaires:  $\text{MMn}_6\text{Sn}_6$  ( $\text{M} = \text{Sc}, \text{Y}, \text{Sm}, \text{Gd}-\text{Tm}, \text{Lu}$ ) ET  $\text{ScFe}_6\text{Sn}_6$ . *Mater. Res. Bull.* **1988**, *23*, 1629–1633.
- 701 (24) Clatterbuck, D. M.; Gschneidner, K. A. Magnetic Properties of  $\text{RMn}_6\text{Sn}_6$  ( $\text{R} = \text{Tb}, \text{Ho}, \text{Er}, \text{Tm}, \text{Lu}$ ) Single Crystals. *J. Magn. Magn. Mater.* **1999**, *207*, 78–94.
- 704 (25) Malaman, B.; Venturini, G.; Welter, R.; Sanchez, J. P.; Vulliet, P.; Ressouche, E. Magnetic Properties of  $\text{RMn}_6\text{Sn}_6$  ( $\text{R} = \text{Gd}-\text{Er}$ ) Compounds From Neutron Diffraction and Mössbauer Measurements. *J. Magn. Magn. Mater.* **1999**, *202*, 519–534.
- 708 (26) Ma, W.; Xu, X.; Yin, J.-X.; Yang, H.; Zhou, H.; Cheng, Z.-J.; Huang, Y.; Qu, Z.; Wang, F.; Hasan, M. Z.; Jia, S. Rare Earth Engineering in  $\text{RMn}_6\text{Sn}_6$  ( $\text{R}=\text{Gd}-\text{Tm}, \text{Lu}$ ) Topological Kagome Magnets. *Phys. Rev. Lett.* **2021**, *126*, No. 246602.
- 712 (27) Weiland, A.; Eddy, L. J.; McCandless, G. T.; Hodovanets, H.; Paglion, J.; Chan, J. Y. Refine Intervention: Characterizing Disordered  $\text{Yb}_{0.5}\text{Co}_3\text{Ge}_3$ . *Cryst. Growth. Des.* **2020**, *20*, 6715–6721.
- 715 (28) Wang, Y.; McCandless, G. T.; Wang, X.; Thanabalasingam, K.; Wu, H.; Bouwmeester, D.; van der Zant, H. S. J.; Ali, M. N.; Chan, J. Y. Electronic Properties and Phase Transition in the Kagome Metal  $\text{Yb}_{0.5}\text{Co}_3\text{Ge}_3$ . *Chem. Mater.* **2022**, *34*, 7337–7343.
- 719 (29) Wang, C.; Liu, S.; Jeon, H.; Jia, Y.; Cho, J.-H. Charge Density Wave and Superconductivity in the Kagome Metal  $\text{CsV}_3\text{Sb}_5$  Around a Pressure-Induced Quantum Critical Point. *Phys. Rev. Mater.* **2022**, *6*, No. 094801.
- 723 (30) Sinha, M.; Vivanco, H. K.; Wan, C.; Siegler, M. A.; Stewart, V. J.; Pogue, E. A.; Pressley, L. A.; Berry, T.; Wang, Z.; Johnson, I.; Chen, M.; Tran, T. T.; Phelan, W. A.; McQueen, T. M. Twisting of 2D Kagomé Sheets in Layered Intermetallics. *ACS Central Science* **2021**, *7*, 1381–1390.
- 728 (31) Avila, M. A.; Takabatake, T.; Takahashi, Y.; Bud'ko, S. L.; Canfield, P. C. Direct Observation of Fe spin Reorientation in Single-Crystalline  $\text{YbFe}_6\text{Ge}_6$ . *J. Phys.: Condens. Matter* **2005**, *17*, 6969.
- 731 (32) Cadogan, J. M.; Ryan, D. H. A Study on the Magnetic Behaviour of Polymorphic  $\text{YbFe}_6\text{Ge}_6$ . *J. Phys.: Condens. Matter* **2010**, *22*, No. 016009.
- 734 (33) Canfield, P. C.; Fisk, Z. Growth of Single Crystals From Metallic Fluxes. *Philos. Mag. B* **1992**, *65*, 1117–1123.
- 736 (34) Canfield, P. C.; Kong, T.; Kaluarachchi, U. S.; Jo, N. H. Use of Frit-Disc Crucibles for Routine and Exploratory Solution Growth of Single Crystalline Samples. *Philos. Mag.* **2016**, *96*, 84–92.
- 739 (35) Krause, L.; Herbst-Irmer, R.; Sheldrick, G. M.; Stalke, D. Comparison of Silver and Molybdenum Microfocus X-ray Sources for Single-Crystal Structure Determination. *J. Appl. Crystallogr.* **2015**, *48*, 3–10.
- 743 (36) Sheldrick, G. Crystal Structure Refinement with SHELXL. *Acta Crystallogr. C* **2015**, *71*, 3–8.
- 745 (37) Bravo, M.; McCandless, G. T.; Baumbach, R. E.; Wang, Y.; Ali, M. N.; Chan, J. Y. Crystal Growth and Physical Properties of Hybrid  $\text{CoSn}-\text{YCo}_6\text{Ge}_6$  Structure Type  $\text{Ln}_x\text{Co}_3(\text{Ge}_{1-y}\text{Sn}_y)_3$  ( $\text{Ln} = \text{Y}, \text{Gd}$ ). *Inorg. Chem.* **2023**, *62*, 18049–18055.
- 748 (38) Mazet, T.; Ihou-Mouko, H.; Ryan, D. H.; Voyer, C. J.; Cadogan, J. M.; Malaman, B. Valence Change and Magnetic Order in  $\text{YbMn}_6\text{Ge}_6\text{-xSn}_x$ . *J. Phys.: Condens. Matter* **2010**, *22*, No. 116005.
- 751 (39) Venturini, G. Filling the  $\text{CoSn}$  Host-Cell: the  $\text{HfFe}_6\text{Ge}_6$ -type and the Related Structures. *Z. Kristallogr. - New Cryst. Struct.* **2006**, *221*, 511–520.
- 754 (40) Baber, W. G.; Mott, N. F. The Contribution to the Electrical Resistance of Metals from Collisions between Electrons. *Proc. R. Soc. London, Ser. A* **1937**, *158*, 383–396.
- 757 (41) Wiser, N. The Electrical Resistivity of the Simple Metals. *Contemporary Physics* **1984**, *25*, 211–249.
- 759 (42) Tran, V. H.; Paschen, S.; Rabis, A.; Baenitz, M.; Steglich, F.; du Plessis, P. D. V.; Strydom, A. M.  $\text{U}_2\text{Ru}_2\text{Sn}$ : a New Kondo Insulator? *Phys. B* **2002**, *312-313*, 215–217.
- 762 (43) Braun, T.; Hlukhyy, V. Structural Order-Disorder in  $\text{CaFe}_6\text{Ge}_6$  and  $\text{Ca}_{1-x}\text{Co}_x\text{Ge}_6$ . *J. Solid State Chem.* **2023**, *318*, No. 123742.
- 764 (44) Welberry, T. R.; Butler, B. D. Diffuse X-ray Scattering from Disordered Crystals. *Chem. Rev.* **1995**, *95*, 2369–2403.
- 766 (45) Welberry, T. R.; Weber, T. One Hundred Years of Diffuse Scattering. *Cryst. Rev.* **2016**, *22*, 2–78.
- 768 (46) Proffen, T. Analysis of Occupational and Displacive Disorder using the Atomic Pair Distribution Function: A Systematic Investigation. *Z. Kristallogr. - New Cryst. Struct.* **2000**, *215*, 661–668.
- 771 (47) Zaharkof, O.; Cervellino, A.; Estermann, M.; Schobinger-Papamantellos, P. Structure of the Microdomain Boundaries in  $\text{RFe}_6\text{Ge}_6$  ( $\text{R} = \text{Tb}, \text{Ho}$  or  $\text{Er}$ ) Crystals from Diffuse X-ray Scattering. *Philos. Mag. A* **2000**, *80*, 27–47.
- 775 (48) Oleksyn, O. Y.; Böhm, H. Ordering in  $\text{DyFe}_6\text{Sn}_6$  Studied by Conventional X-ray Single Crystal Diffraction. *Z. Kristallogr. - Cryst. Mater.* **1998**, *213*, 270–274.
- 778 (49) Fredrickson, D. C.; Lidin, S.; Venturini, G.; Malaman, B.; Christensen, J. Origins of Superstructure Ordering and Incommensurability in Stuffed  $\text{CoSn}$ -Type Phases. *J. Am. Chem. Soc.* **2008**, *130*, 8195–8214.
- 782 (50) Mruz, O. Y.; Starodub, P. K.; Bodak, O. I. New Representatives of the Structure Type  $\text{YCo}_6\text{Ge}_6$ . *Dop. Akad. Nauk Ukrain. RSR* **1984**, *Ser B12*, 45–47.
- 785 (51) Venturini, G. Crystallographic and Magnetic Properties of  $\text{TbFe}_6\text{Ge}_6\text{-xGa}_x$  Compounds ( $0.5 \leq x \leq 3.5$ ). *J. Alloys Compd.* **2001**, *329*, 8–21.
- 788 (52) Ihou-Mouko, H.; Venturini, G. Crystallographic Properties of  $\text{ErFe}_6\text{Sn}_6\text{-xGa}_x$  Compounds ( $0 < x < 6$ ). *J. Alloys Compd.* **2005**, *396*, 59–63.
- 791 (53) Mazet, T.; Welter, R.; Malaman, B. A Study of the New Ferromagnetic  $\text{YbMn}_6\text{Sn}_6$  Compound by Magnetization and Neutron Diffraction Measurements. *J. Magn. Magn. Mater.* **1999**, *204*, 11–19.
- 794 (54) Magnette, A.; Vernière, A.; Venturini, G.; Eichenberger, L.; Malaman, B.; Mazet, T. Crystal and Magnetic Properties of  $\text{YbMn}_{6-y}\text{Fe}_y\text{Sn}_6$  ( $y \leq 1$ ). *J. Magn. Magn. Mater.* **2018**, *458*, 19–22.
- 797 (55) Fedyna, M. F.; Skolozdra, R. V.; Gorelenko, Y. K. Magnetic and electric properties of  $\text{RCo}_6\text{Ge}_6$  ( $\text{R} = \text{Y}, \text{Dy}, \text{Er}-\text{Lu}$ ). *Neorg. Mater.* **1999**, *35*, 461–463.
- 800 (56) Cadogan, J. M.; Ryan, D. H. Independent Magnetic Ordering of the Rare-Earth (R) and Fe Sublattices in the  $\text{RFe}_6\text{Ge}_6$  and  $\text{RFe}_6\text{Sn}_6$  series. *J. Alloys Compd.* **2001**, *326*, 166–173.
- 803 (57) Oleksyn, O.; Schobinger-Papamantellos, P.; Rodríguez-Carvajal, J.; Brück, E.; Buschow, K. H. J. Crystal Structure and Magnetic Ordering in  $\text{ErFe}_6\text{Ge}_6$  studied by X-ray, Neutron Diffraction and Magnetic Measurements. *J. Alloys Compd.* **1997**, *257*, 36–45.
- 807 (58) Cadogan, J. M.; Ryan, D. H.; Swainson, I. P. Neutron Diffraction Determination of the Magnetic Structure of  $\text{DyFe}_6\text{Ge}_6$ . *J. Phys.: Condens. Matter* **2000**, *12*, 8963.
- 810 (59) Schobinger-Papamantellos, P.; Buschow, K. H. J.; de Boer, F. R.; Ritter, C.; Isnard, O.; Fauth, F. The Fe Ordering in  $\text{RFe}_6\text{Ge}_6$  Compounds with Non-Magnetic R ( $\text{R} = \text{Y}, \text{Lu}, \text{Hf}$ ) Studied by Neutron Diffraction and Magnetic Measurements. *J. Alloys Compd.* **1998**, *267*, 59–65.

- 816 (60) Häggström, L.; Ericsson, T.; Wäppling, R.; Chandra, K. Studies  
817 of the Magnetic Structure of FeSn Using the Mössbauer Effect. *Phys.*  
818 *Scr.* **1975**, *11*, 47–54.
- 819 (61) Yang, T.-H.; Gao, S.; Zhang, Y.; Olds, D.; Meier, W. R.; Stone,  
820 M. B.; Sales, B. C.; Christianson, A. D.; Zhang, Q. Simultaneous  
821 Development of Antiferromagnetism and Local Symmetry Breaking in  
822 a Kagome Magnet (Co<sub>0.45</sub>Fe<sub>0.55</sub>)Sn. *J. Am. Chem. Soc.* **2024**, *146*,  
823 34374–34382.
- 824 (62) Li, V. M.; Adams, M.; Shatruk, M. Generating Ferromagnetic  
825 Kagomé Metal by Magnetic Phase Boundary Mapping in the  
826 YFe<sub>6</sub>Ge<sub>6</sub>–YCo<sub>6</sub>Ge<sub>6</sub> System. *Chem. Mater.* **2025**, *37*, 247.